

Genetic Algorithm for Inferring Model Parameters for Flux Transport Dynamo Simulation

Y. SHIMIZU ¹ AND H. HOTTA ¹

¹*Institute for Space-Earth Environmental Research, Nagoya University, Furo-cho, Chikusa-ku, Nagoya, Aichi 464-8601, Japan*

ABSTRACT

The Sun exhibits an 11-year cyclic variation, maintained by dynamo action in the solar interior. Mean-field flux transport dynamo models have successfully reproduced most of the features observed in solar cycles, while the model includes many free parameters, such as the speed of the meridional flow and the amplitude of the poloidal field generation. Inferring these free parameters is on demand because they correspond to the solar interior condition. We suggest a novel method for inferring the free parameters using a genetic algorithm. At each generation, we evaluate the fitness of our simulation against the observational data and optimize the parameters. We apply our method to the observed solar cycle data from 1723 to 2024 and successfully reproduce the observations from both qualitative and quantitative perspectives. We expect our method to be applicable to sunspot numbers, even those obtained from isotope data and historical documents, in the future, to better understand past solar interior dynamics.

Keywords: Solar physics (1476) — Solar cycle (1487) — Solar dynamo (2001) — Algorithms (1883) — Magnetohydrodynamical simulations (1996)

1. INTRODUCTION

The number of sunspots varies with the 11-year cycle. The cyclic behavior exhibits many rules, such as equatorward migration of sunspot latitude (E. W. Maunder 1904), and a symmetric rule for polarity of sunspot pairs about the equator (G. E. Hale et al. 1919). Elucidating these features is one of the most important research topics in solar physics (see review by P. Charbonneau 2020). In addition to the regular cyclic behavior, it is known that the cycle amplitude and period depend on the individual cycle (D. H. Hathaway 2010). The cycle and the longer-scale variation can be attributed to the magnetic field generation, i.e., the dynamo action, in the solar interior (B. B. Karak 2023).

Numerical simulations play a key role in addressing the origin and the variation of the sunspot cycle, as direct observation of the solar deeper layers, where the dynamo action is thought to occur, is extremely limited. Numerical simulation enables us to examine the solar interior dynamics and are considered an effective solution for investigating solar activity. The flux transport dynamo is one of the most promising models for reproducing the solar cycle and its features (A. R. Choudhuri

et al. 1995; M. Dikpati & P. Charbonneau 1999). In the model, the pre-existing poloidal field is stretched by differential rotation to produce the toroidal field around the base of the convection zone (Ω -effect: E. N. Parker 1955). Then the toroidal field rises to the surface due to magnetic buoyancy and/or thermal convection (Y. Fan 2021). During the flux rise, the Coriolis force bends the field to produce a poloidal magnetic field around the surface (so called the Babcock-Leighton α -effect: H. W. Babcock 1961; R. B. Leighton 1969). The generated poloidal field is transported by the meridional flow and turbulent diffusion (H. Hotta & T. Yokoyama 2010). The flux transport dynamo simulation is a mean-field model that includes several free parameters, such as the meridional flow speed and the amplitude of the Babcock–Leighton α -effect. There have been several attempts to infer the free parameters and reproduce the observational feature of the sunspot cycle. For example, A. Lemerle & P. Charbonneau (2017) constructed a solar dynamo model optimized for cycle 21, in which a genetic algorithm tuned the input free parameters to match the observations, and the model was then applied to reproduce solar cycles and explore long-term variability. B. B. Karak (2010) evaluate time variations in the meridional flow speed manually to reproduce changes in cycle period and amplitude, as well as the Maunder Minimum.

In the observational aspect, isotope analyses and historical documents research to understand the past solar activity have significantly progressed in the past two decades. They are studying solar activity from an ancient era for which no precise records are available. For example, [H. Miyahara et al. \(2004\)](#) carried out a high-precision analysis of carbon-14 in annual ring data during the Maunder Minimum and suggested that even during the grand minimum, the dynamo may not have ceased and the solar polarity reversal may have been maintained. [H. Hayakawa \(2025\)](#) presents an example of research that utilizes historical documents from the 17th to 18th centuries to reconstruct long-term solar variability, providing fundamental data sets for the reconstruction of ancient solar activity and further supporting the hemispheric asymmetry during the Maunder Minimum.

Considering the recent rapid accumulation of the sunspot and solar activity data, an automatic method(s) to evaluate the solar internal dynamics is in high demand. [A. Lemerle & P. Charbonneau \(2017\)](#) adapted a similar approach, but they obtained constant parameters in time. In reality, we expect most things to depend on time, and we try to infer the temporal variation of parameters in this study.

This paper is structured as follows: The methods for the numerical simulation and the genetic algorithm are explained in Section 2. The results for validating our method and the application to the observational data are shown in 3.

2. METHOD

2.1. Numerical model

We solve the axisymmetric induction equation in spherical coordinates (r, θ, ϕ) with the kinematic assumption, i.e., the flow field \mathbf{u}_p is given. The magnetic field \mathbf{B} is decomposed to the poloidal mean field $\mathbf{B}_p = \nabla \times [A_\phi(r, \theta)\mathbf{e}_\phi]$ and the toroidal field $B_\phi\mathbf{e}_\phi$, and our equations can be written as (e.g., [M. Dikpati & P. Charbonneau 1999](#))

$$\begin{aligned} \frac{\partial A_\phi}{\partial t} + \frac{1}{r \sin \theta} (\mathbf{u}_p \cdot \nabla) (r \sin \theta A_\phi) \\ = \eta \left(\nabla^2 - \frac{1}{r^2 \sin^2 \theta} \right) A_\phi + S(r, \theta; B_\phi), \end{aligned} \quad (1a)$$

$$\begin{aligned} \frac{\partial B_\phi}{\partial t} + \frac{1}{r} \left[\frac{\partial}{\partial r} (r u_r B_\phi) + \frac{\partial}{\partial \theta} (u_\theta B_\phi) \right] \\ = r \sin \theta (\mathbf{B}_p \cdot \nabla) \Omega - \frac{1}{r} \frac{\partial \eta}{\partial r} \frac{\partial}{\partial r} (r B_\phi) \\ + \eta \left(\nabla^2 - \frac{1}{r^2 \sin^2 \theta} \right) B_\phi, \end{aligned} \quad (1b)$$

where \mathbf{u}_p represents the meridional flow velocity ($\mathbf{u}_p = u_r \mathbf{e}_r + u_\theta \mathbf{e}_\theta$), Ω is the angular velocity representing the differential rotation, and $S(r, \theta; B_\phi)$ shows the Babcock-Leighton α -effect source term. When the magnetic field is generated around the base of the convection zone, the corresponding magnetic field is generated around the surface. η represents turbulent diffusivity. In this study, we basically follow the settings of [L. Jouve et al. \(2008\)](#) (see their equations (7) and (8)). While the compression term $-\mathbf{B} \nabla \cdot \mathbf{u}$ is ignored in their study, we do not do so.

Equations (1) are solved on the meridional plane ($0 \leq \theta \leq \pi$). The radial domain extends $0.65R_\odot < r < R_\odot$, where $R_\odot = 6.96 \times 10^{10}$ cm is the solar radius.

The bottom boundary at $r = 0.65R_\odot$ is set to be a perfect conductor as

$$A_\phi = 0 \quad \text{and} \quad \frac{\partial(rB_\phi)}{\partial r} = 0. \quad (2)$$

The upper boundary condition at $r = R_\odot$: we smoothly match the magnetic field to an external potential field, i.e., we assume that the exterior of the Sun is a vacuum and current-free. This condition is expressed as

$$\left(\nabla^2 - \frac{1}{r^2 \sin^2 \theta} \right) A_\phi = 0 \quad \text{and} \quad B_\phi = 0. \quad (3)$$

At $\theta = 0$ and $\theta = \pi$ boundaries, we impose the regularity conditions as

$$A_\phi = 0 \quad \text{and} \quad B_\phi = 0. \quad (4)$$

We employ the second-order space-centered derivative and second-order Total Variation Diminishing (TVD) Runge-Kutta method for time integration. For details of TVD Runge-Kutta method, please refer to the appendix. No artificial viscosity is included. The calculation is stabilized with the turbulent diffusivity. Our simulation is consistent with the results of a solar mean field dynamo benchmark test ([L. Jouve et al. 2008](#)). We use the formulations introduced in [L. Jouve et al. \(2008\)](#) for the following ingredients of the meridional flow, the α -effect source term, and the turbulent diffusivity.

The profile of differential rotation Ω is defined as

$$\Omega(r, \theta) = \Omega_c + \frac{1}{2} \left[1 + \operatorname{erf} \left(\frac{r - r_c}{d} \right) \right] (\Omega_e - \Omega_c - c_2 \cos^2 \theta), \quad (5)$$

where $\Omega_e/2\pi = 460$ nHz, $\Omega_c = 0.92\Omega_e$, $c_2 = 0.2\Omega_e$, $r_c = 0.7R_\odot$, $d = 0.02R_\odot$. In our expression, the core rotates with Ω_c and the thickness of the tachocline at $r = r_c$ is d . This angular velocity distribution roughly reproduces the observational result by helioseismology ([J. Schou et al. 1998](#); [H. Hotta et al. 2023](#)).

The profile of meridional flow is given as

$$u_r(r, \theta) = -u_0 \frac{2(R_\odot - r_b)}{\pi r} \frac{(r - r_b)^2}{(R_\odot - r_b)^2} \times \sin\left(\pi \frac{r - r_b}{R_\odot - r_b}\right) (3 \cos^2 \theta - 1), \quad (6a)$$

$$u_\theta(r, \theta) = u_0 \left[\frac{3r - r_b}{R_\odot - r_b} \sin\left(\pi \frac{r - r_b}{R_\odot - r_b}\right) + \frac{r\pi}{R_\odot - r_b} \frac{r - r_b}{R_\odot - r_b} \cos\left(\pi \frac{r - r_b}{R_\odot - r_b}\right) \right] \times \frac{2(R_\odot - r_b)}{\pi r} \frac{r - r_b}{R_\odot - r_b} \cos \theta \sin \theta, \quad (6b)$$

where $r_b = 0.65R_\odot$ and the amplitude of the meridional flow u_0 is a parameter to be varied and inferred in this study. The flow is set to vanish at $r = 0.65R_\odot$.

With the Babcock–Leighton α effect, the source term is defined as

$$S(r, \theta; B_\phi) = \frac{s_0}{2} \left[1 + \operatorname{erf}\left(\frac{r - r_1}{d_1}\right) \right] \left[1 - \operatorname{erf}\left(\frac{r - R_\odot}{d_1}\right) \right] \times \left[1 + \left(\frac{B_\phi(r_c, \theta, t)}{B_0} \right)^2 \right]^{-1} \cos \theta \sin \theta B_\phi(r_c, \theta, t), \quad (7)$$

where $r_1 = 0.95R_\odot$, $d_1 = 0.01R_\odot$. The amplitude of the source term s_0 is another parameter to be varied and inferred in this study. To prevent the magnetic field from growing exponentially without bounds, we introduce a nonlinear quenching term $[1 + (B_\phi(r_c, \theta, t)/B_0)^2]^{-1}$ with B_0 being an arbitrary normalization constant. In this paper, B_ϕ and A_ϕ are shown as values normalized by B_0 . We note some previous research for the tilt and the latitude of sunspots support the existence of the quenching in the Babcock-Leighton process (e.g. B. K. Jha et al. 2020; J. Jiang 2020; B. Dey et al. 2025).

Here, we emulate the observed cycle-to-cycle variation by adjusting u_0 and s_0 , because the prevailing theory shows that the irregularity of the solar cycle comes from the fluctuations in the Babcock-Leighton α effect and the meridional circulation (A. R. Choudhuri 1992; A. R. Choudhuri & B. B. Karak 2009; B. B. Karak & A. R. Choudhuri 2013). Thus, we consider the time variations of the meridional flow speed u_0 and the source term amplitude s_0 . A sine-series expansion controls the time dependence of these parameters as

$$u_0(t) = \frac{a_s^u(T_e - t) + a_e^u(t - T_s)}{T_e - T_s} + \sum_{l=1}^{l_{\max}} a_l^u \sin l\omega t, \quad (8a)$$

$$s_0(t) = \frac{a_s^s(T_e - t) + a_e^s(t - T_s)}{T_e - T_s} + \sum_{l=1}^{l_{\max}} a_l^s \sin l\omega t. \quad (8b)$$

where T_s and T_e are the start and end time of inference. We set $l_{\max} = 4$ to compromise expressiveness and inversion difficulty. Note that $l = 3$ is excluded to determine the start and end points of the parameter's time variation by a_s^u , a_e^u , a_s^s and a_e^s .

The angular frequency ω is defined as

$$\omega = \frac{2\pi}{2(T_e - T_s)}, \quad (9)$$

The profile of turbulent diffusivity is given as

$$\eta(r) = \eta_c + \frac{1}{2}(\eta_t - \eta_c) \left[1 + \operatorname{erf}\left(\frac{r - r_c}{d}\right) \right], \quad (10)$$

where $\eta_c = 1 \times 10^9 \text{ cm}^2 \text{ s}^{-1}$, $\eta_t = 1 \times 10^{11} \text{ cm}^2 \text{ s}^{-1}$. We assume that the diffusivity in the convection zone is dominated by η_t whereas below the tachocline, turbulence rapidly weakens and diffusion becomes about η_c .

2.2. Genetic algorithm(GA)

We use Genetic Algorithm (GA) to obtain the time variation of the parameters $s_0(t)$ and $u_0(t)$, i.e., coefficients in equation (8).

We first randomly prepare 30 tuples of coefficients a_n (Figure 1a). Each tuple is called an ‘‘individual.’’ The group of individuals is referred to as the ‘‘population.’’ The initial population generated in this way is referred to as the 0-th generation. Our defined fitness parameter evaluates each individual. We use time series sunspot number (SSN) data $S_{\text{GT}}(t_i)$ as a measure of solar cycles. The fitness parameter is calculated with the observed/simulated ground truth data $S_{\text{GT}}(t_i)$ and simulated data $S_{\text{sim}}(t_i)$. We define the fitness parameter as

$$F = \alpha r_{\text{sunspot}} - (1 - \alpha) e_{\text{sunspot}}, \quad (11)$$

where the weight is $\alpha = 0.9$. r_{sunspot} is the correlation coefficient given as

$$r_{\text{sunspot}} = \frac{\sum_i S'_{\text{GT}}(t_i) S'_{\text{sim}}(t_i)}{\sqrt{\sum_i S'^2_{\text{GT}}(t_i) \sum_i S'^2_{\text{sim}}(t_i)}}, \quad (12)$$

where $\langle S_* \rangle$ denote the ensemble average and $S'_* = S_* - \langle S_* \rangle$. e_{sunspot} is the normalized mean square error given as

$$e_{\text{sunspot}} = \frac{\sum_i [S_{\text{GT}}(t_i) - S_{\text{sim}}(t_i)]^2}{\sum_i S^2_{\text{GT}}(t_i)}. \quad (13)$$

As for SSN, we adopt the square of the toroidal field (B_ϕ^2) at latitude 15° at the base of the convection zone (M. Dikpati & P. Charbonneau 1999) defined as:

$$\text{SSN} = \gamma B_\phi^2(r = 0.7R_\odot, \theta = 15^\circ), \quad (14)$$

where the coefficient is $\gamma = 5.865$ in this study.

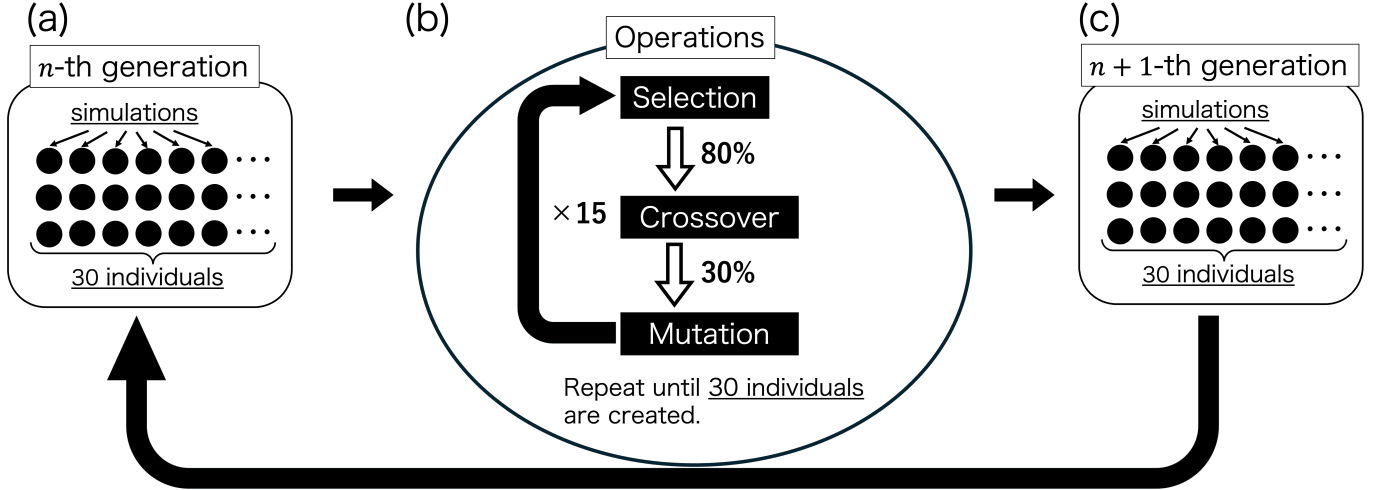


Figure 1. Overview of our Genetic Algorithms. Panel(a) represents n -th generation. The black filled circles indicate individuals. Panel (b) represents the Genetic Algorithms operations. After two individuals are selected, crossover and mutation are performed with 80% and 30% probability, respectively. We repeat these operations until 30 individuals are created. Panel(c) represents the $n + 1$ -th generation. By repeating (a) to (c), leads to the optimal solution.

Then, we generate the next generation population, where GA undergoes three genetic operators: “selection,” “crossover,” and “mutation” (Figure 1b). These three operations are regarded as a “regular set.” A regular set operation generates two individuals for the next generation (Figure 1c). We repeat the regular set to generate 30 next-generation individuals. We explain the actual operations of selection, crossover, and mutation, and the methods employed in this study.

Selection is an operator that chooses two individuals as parents for the next generation. We select individuals based on our fitness parameter F . We adopt an adaptive selection pressure scheme, which dynamically adjusts the strength of selection pressure, i.e., how strongly better-adapted individuals are favored, according to the progress of GA (A. Eiben et al. 2006). We use tournament selection. In this method, m individuals are randomly chosen from the population, and the top two are selected as parents. The tournament size m is determined by the selection pressure. The selection pressure controls both “progress” and “diversity” of the optimization. We evaluate the progress of GA using the relative change rate in the best fitness parameter ΔF_n and diversity D_n as indicators. ΔF_n is defined as

$$\Delta F_n = \frac{|F_n - F_{n-1}|}{|F_{n-1}|}, \quad (15)$$

where F_n represents the best fitness parameter F of the n -th generation. We use the mean of the standard deviations of all parameters after normalization as a diversity measure. Each parameter is first normalized by its

range,

$$\hat{x}_{i,n}^{(k)} = \frac{x_{i,n}^{(k)} - \min(x_{i,n}^{(k)})}{\max(x_{i,n}^{(k)}) - \min(x_{i,n}^{(k)})}, \quad (16)$$

where $x_{i,n}^{(k)}$ is a parameter for the inference with the parameter kind k , i.e., a_0^s , a_0^u , a_1^s , and $a_1^u \dots$, individual identifier i and the generation n . Then our diverse measure is defined as

$$D_n = \frac{1}{N_k} \sum_{k=1}^{N_k} \sqrt{\frac{\sum_{i=1}^{N_p} (\hat{x}_{i,n}^{(k)} - \langle \hat{x}_{i,n}^{(k)} \rangle)^2}{N_p}}, \quad (17)$$

where N_k is the number of parameter kind and N_p is the population size. Given thresholds $\epsilon_{\text{fit}} = 0.005$ and $\epsilon_{\text{div}} = 0.10$, the tournament size m is set by

$$m = \begin{cases} 3 & (\Delta F_n < \epsilon_{\text{fit}} \text{ and } D_n < \epsilon_{\text{div}}) \\ 7 & (\Delta F_n < \epsilon_{\text{fit}} \text{ and } D_n > \epsilon_{\text{div}}) \\ 5 & (\Delta F_n > \epsilon_{\text{fit}}) \end{cases} \quad (18)$$

For example, when ΔF_n and D_n are small, we regard the GA as having converged on a local optimum. In this case, we set the tournament size to 3 to increase the randomness and recover diversity.

Crossover is an operator that creates two new individuals by exchanging part of the parameters of the parents in the Binary-coded GA. However, in Real-coded GA, crossover is designed to generate children in the continuous search space built on the parameters of the parents. In this study, we adopt Simulated Binary Crossover

(SBX) suggested in (K. Deb & H.-G. Beyer 2001). SBX is a Real-coded GA crossover method that incorporates elements of a single-point crossover from binary-coded GAs, where children are generated according to a probability distribution with peaks near the values of the parents. Two $n + 1$ -th generation children, $x_{c_1, n+1}^{(k)}$, and $x_{c_2, n+1}^{(k)}$, are generated from two parents in n -th generation $x_{p_1, n+1}^{(k)}$, and $x_{p_2, n+1}^{(k)}$ as

$$x_{c_1, n+1}^{(k)} = \frac{1}{2} \left[(1 + \beta_{\text{CO}})x_{p_1, n}^{(k)} + (1 - \beta_{\text{CO}})x_{p_2, n}^{(k)} \right], \quad (19a)$$

$$x_{c_2, n+1}^{(k)} = \frac{1}{2} \left[(1 - \beta_{\text{CO}})x_{p_1, n}^{(k)} + (1 + \beta_{\text{CO}})x_{p_2, n}^{(k)} \right]. \quad (19b)$$

β_{CO} determines the probability distribution and is given as

$$\beta_{\text{CO}} = \begin{cases} (2u)^{\frac{1}{\eta_{\text{CO}}+1}}, & \text{if } u \leq 0.5, \\ \left[\frac{1}{2(1-u)} \right]^{\frac{1}{\eta_{\text{CO}}+1}}, & \text{otherwise.} \end{cases} \quad (20)$$

where u is a uniform random number ($0 \leq u \leq 1$), η_{CO} is the distribution index, which is a free nonnegative parameter. A large η_{CO} gives a high probability of being near the parents, and a small η_{CO} allows distant solutions from the parents. In this study, we set $\eta_{\text{CO}} = 2$.

Mutation is an operator that introduces random modifications to the part of parameters to maintain diversity and to avoid premature convergence to local optima. While crossover explores the search space by combining parental information, mutation plays a complementary role by perturbing individuals, thereby enhancing the exploration of unexplored regions. In this study, we adopt the Gaussian Mutation (e.g. H.-G. Beyer & H.-P. Schwefel 2002).

In the algorithm, the mutation occurs under the Gaussian probability function centered in parameter $x_{i, n}^{(k)}$, and whose width σ is 10% of the absolute value of the parameter, i.e., $\sigma = 0.1 \left| x_{i, n}^{(k)} \right|$.

We note that the crossover and mutation are performed with probabilities of 80% and 30%, respectively. If they are not performed, the selected individuals are passed without any modification.

The initial conditions of our numerical simulation are also prepared in our GA procedure. We first carry out a regular simulation with $u_0 = 695 \text{ cm s}^{-1}$ and $s_0 = 50 \text{ cm s}^{-1}$. We can reproduce the average solar cycle, characterized by approximately 166 sunspots at maximum and a period of 11 years. The initial condition of this simulation is an arbitrarily large-scale field

given as

$$A_\phi = \begin{cases} 0 & \text{for } r < 0.7R_\odot, \\ \frac{\sin \theta}{r^2} & \text{for } \geq 0.7R_\odot, \end{cases} \quad (21)$$

$$B_\phi = 0. \quad (22)$$

The simulation was run for 250 years, and representative results are shown in Figure 2. Figure 2e shows the butterfly diagram derived from simulation results. It exhibits characteristics and shapes consistent with observations, such as polarity reversing every 11 years and the polarity being opposite in the northern and southern hemispheres.

Then, we use the data from the regular simulation with a cycle minimum as an initial condition and restart numerical simulations with parameters $u_0 = a_s^u$ and $s_0 = a_s^s$ obtained in the GA procedure. This simulation continues in a cycle minimum of around 80 years. The data in the cycle minimum is used as the initial condition for the main GA procedure. Therefore, initial conditions vary between individuals, and the methodology employed in this study also explores optimal initial conditions. We note that due to the method of setting initial conditions, parameter inference always begins at a minimum.

3. RESULT

3.1. Method validation with simulation generated data

We evaluate the ability of our method by inferring the free parameters for ground truth data generated by numerical simulations in this section. We can control the parameters u_0 and s_0 independently and evaluate the ability of our estimation. The ground truth data is the simulation results for five cycles with both u_0 and s_0 varying over time. The meridional flow basically determines the cycle period. The faster meridional flow tends to cause a shorter solar cycle period, and vice versa. Optimization often falls into a local optimum when we infer parameters for meridional flow u_0 and α effect s_0 simultaneously. Thus, we infer them using the following procedure:

Step 1: Time dependent u_0 and fixed s_0 are inferred.

Step 2: Time dependent s_0 is inferred with u_0 obtained in Step 1.

Figures 3a, c, and e show the results of Step 1. Figure 3a shows the SSNs of the ground truth (red) and the GA inference (blue). While the SSNs at maxima are slightly deviated, the overall structure can be reproduced. The amplitude of the meridional flow are recovered (Figure 3c). While the amplitude of the α -effect s_0

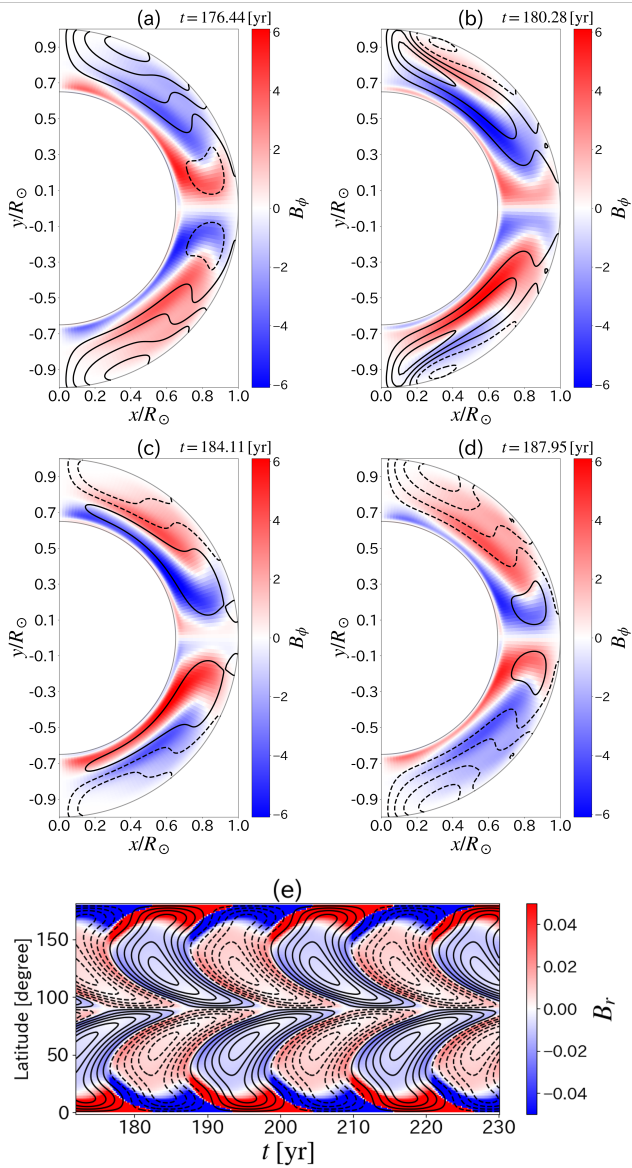


Figure 2. Evolution of the toroidal and poloidal magnetic field components. Panels a, b, c, and d are results separated by intervals of 3.83 years. In panels a-d, the red and blue colors represent the toroidal magnetic field B_ϕ , and the contour lines are magnetic field lines of the poloidal field. The solid and dashed lines indicate clockwise and counterclockwise field. These results are characterized by a cycle period of 22.028 yr. Panel e shows a butterfly diagram for 58.2 years. The color contours represent B_r at the top boundary ($r = R_\odot$), and the contour lines represent B_ϕ around the base of the convection zone $r = 0.7R_\odot$.

is constant over time in Step 1, the amplitude is roughly inferred. The correlation coefficient between the ground truth SSNs and the GA inference is 0.975. The mean absolute percentage error for u_0 and s_0 are 2.87% and 10.89%, respectively. Figures 3b, d, and f show the re-

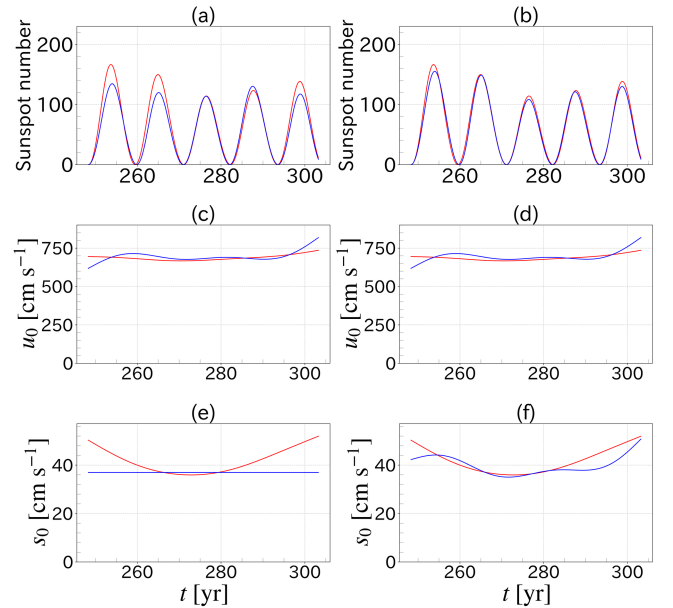


Figure 3. Comparison between the ground truth data generated by the simulation and our inference. Panels a, c, and e (Step 1) show the results of inferring only the time variation of u_0 , and panels b, d, and f show the results of inferring the time variation of s_0 with u_0 obtained in Step 1. Panels a and b show the time variation of SSN. Panels c and d show the time variation of u_0 , and panels e and f show the time variation of s_0 . The red and blue colors show the ground truth and our GA inference, respectively.

sults of Step. 2. Compared with 3a, Step 2 improves the reproduction ability, especially about the amplitude of the SSN (Figure 3b). The sunspot correlation coefficient in Step 2 is 0.995, and the mean absolute percentage error for s_0 is 5.25%, which is reduced from that in Step 1. According to Figure 3f, the trend in the time variation of s_0 can be inferred.

3.2. Application to observation data

We apply our method to observational SSN data from 1723 to 2024 and perform inference of the dynamo parameters u_0 and s_0 (Figure 4). As longer time inference is very challenging, we divide the SSN data into 5-cycle units. Inference is separately applied to each 5-cycle unit. Thus, the results are not continuous. It is preferable to infer as long duration as possible at once. We confirm that inferring with 3 or 4-cycle unit does work. While we expect that longer than 5-cycle unit is also possible, the difficulty of inference increases. As a compromise, we choose the 5-cycle unit.

We conducted the GA with a maximum of 50th generation. While we use the fitness parameter defined in equation (11) for most of the period, we employ a different definition for the period 1775–1833, which corresponds to the Dalton Minimum. The mean square error

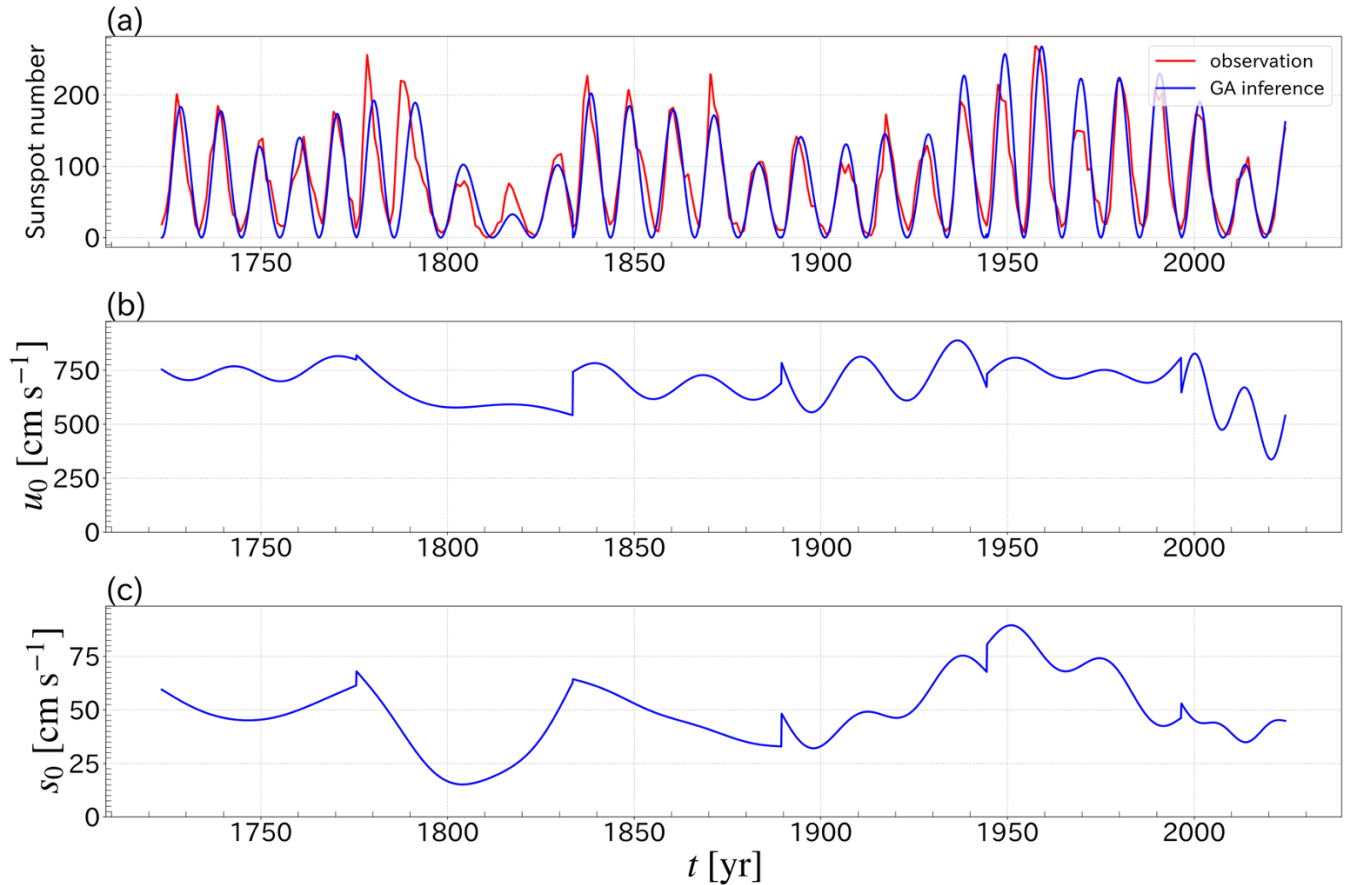


Figure 4. Inference result for the observational data. Panel a shows the time variation of SSN. The red and blue represent the observational data and GA inference, respectively. The observed SSN is yearly mean total sunspot number by SILSO (Sunspot Number Version 2.0 (WDC–SILSO, Royal Observatory of Belgium 2025)). We interpolate the data to achieve 40-day intervals for the inference. Inference is performed every 5 cycles, and we merge all the inferences into a plot. Panels b and c represent the time variations of the inferred u_0 and s_0 , respectively.

for the cycle period is used as the fitness parameter in Step 1. The different definition is used because the original fitness parameter in Step 1 attempts to reproduce the sharp peak fluctuations in the observed data solely through the time variation of u_0 , leading to a local optimum.

We first discuss the overall structure of the inference (Figure 4a). The number of sunspots at the maximum and the periodicity are acceptably reproduced. Figure 4b shows that u_0 fluctuates within the range of -51.1% to $+29.0\%$ of time average while s_0 exhibits a larger fluctuation range (Figure 4c), with fluctuation of -69.1% to $+82.7\%$. We calculate the correlation coefficient between cycle rise time and the peak sunspot number to evaluate the ability of the GA inference in this study. The relation is known as the Waldmeier effect (M. Waldmeier 1935, 1939). In our inferred data, the correlation coefficient is -0.526 , indicating an acceptable relation be-

tween them. We note that the correlation coefficient evaluated with the observed sunspot number is -0.766 .

Then, we examine the results of each 5-cycle unit. The SSN correlation coefficients obtained in chronological order from the oldest data are 0.927 , 0.685 , 0.933 , 0.935 , 0.873 , and 0.974 . Figures 4a and b clearly show that the meridional flow velocity decreased during the Dalton Minimum from 1790 to 1830. H. Miyahara et al. (2021) expected that the meridional flow decreased during a grand minimum (B. B. Karak 2010); our analysis can support this idea. A comparison between Figures 4a and c indicates that s_0 becomes smaller when the SSN is relatively low (around 1750, 1816, and 1905). It is worth noting that the timing of s_0 minimum (1746, 1804, and 1898) is slightly earlier than the timing of sunspot amplitude minimum (1750, 1816, and 1905).

There should be a time lag between the α effect, creating a poloidal magnetic field on the solar surface, and toroidal field generation around the base of the convec-

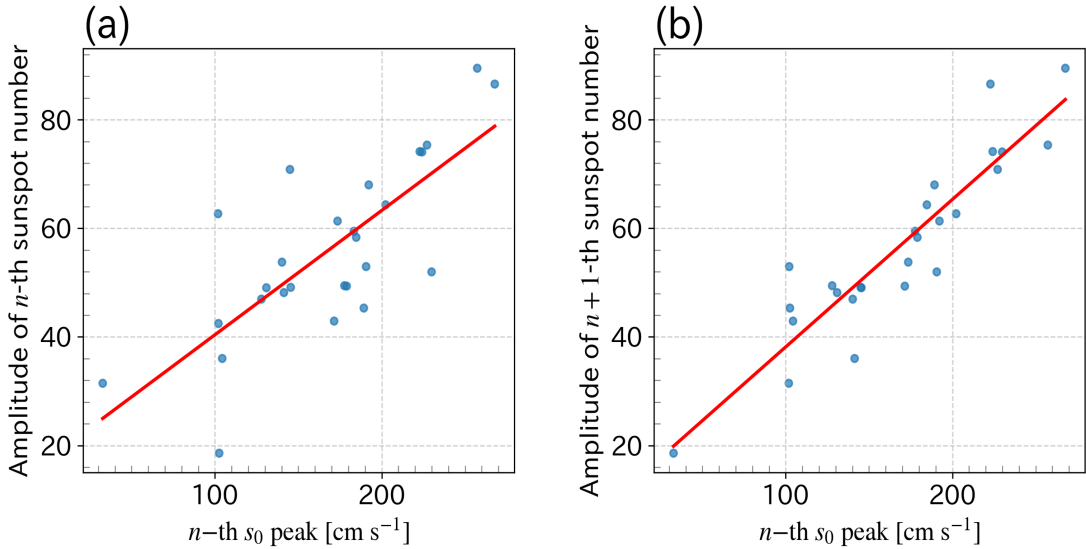


Figure 5. Relation between s_0 and sunspot numbers. Panel a shows a scatter plot of the peak value of s_0 at the n -th cycle and the amplitude of the n -th sunspot number. Panel b shows a scatter plot of the peak value of s_0 at the n -th cycle and the amplitude of the $n+1$ -th sunspot number. The correlation coefficients for the panels a and b are 0.763 and 0.916, indicating a time lag between the poloidal and toroidal field generations.

tion zone by the Ω effect. We evaluate two correlation coefficients. One is that between the peak value of s_0 at the n -th cycle and the amplitude of the n -th sunspot number (Figure 5a). The other is that between the peak value of s_0 at the n -th cycle and the amplitude of the $n+1$ -th sunspot number (Figure 5b). The correlation coefficient for the former and the latter is 0.763 and 0.916, respectively. The better coefficient of the latter partly implies the time lag between the poloidal and toroidal field generations. The somewhat poor correlation value of 0.763 in Figure 5a implies that the solar cycle memory is disturbed by the fluctuations and the toroidal cycle amplitude to poloidal as determined by s_0 value in Figure 5a. It is not strongly correlated as expected for the Sun.

We observe that the amplitude for cycle 20 (1964–1976) has not been precisely reproduced. B. Dey et al. (2025) suggest that the cycle 20’s weakness is due to the reduced tilt angle of the sunspots for cycle 19, which generated a weak polar field and the weak following cycle. The unsuccessful reproduction in our study is thought to stem from an inability to estimate the abrupt change in s_0 during cycle 19.

Figure 6 presents several statistical evaluations of the overall inference results. Figure 6a shows a scatter plot for all corresponding SSN, with a correlation coefficient of 0.876. Data points significantly deviating from the regression line to the lower right correspond to the results around 1784–1798. Figure 6b shows the scatter plot for each cycle period, with a correlation coefficient of 0.566. This value is worse than that in B. B. Karak

(2010) because our optimization does not include the cycle period as a fitness parameter. We intend to optimize the free parameters to reproduce the overall structure of the SSN rather than solely the cycle period. Figure 6c shows a scatter plot of SSN at each maximum, with a correlation coefficient of 0.842. This value is superior to that in B. B. Karak (2010) because we also optimize s_0 .

4. SUMMARY AND DISCUSSION

We develop a method to reproduce the observed solar cycles in numerical simulations, utilizing automatic inference of free parameters. We try to infer the amplitudes of the meridional flow u_0 and the α effect. The temporal evolutions of these are also inferred. These parameters are expanded (Equation (8)) with the sine functions, and the coefficients for these sine functions are inferred. As an inference method, we adopt a GA method. We carry out a number of simulations and evaluate their fitness against ground truth data with certain parameters. Then, the following generation is created using “Selection,” “Crossover,” and “Mutation.” As the generation progresses, the ability of numerical simulations to replicate the observation improves. We apply this method to observational data (1723–2024) and successfully reproduce the overall structure in the time series of SSN. Regarding the time lag between the poloidal and toroidal field generations confirmed from the reproduction and inference results, we can consider exploring the memory of the solar cycle predicted in P. Kumar et al. (2021) for the future work. Several issues remain to be addressed in future studies. The fitness parameter is open to discussion. For example, we consider that

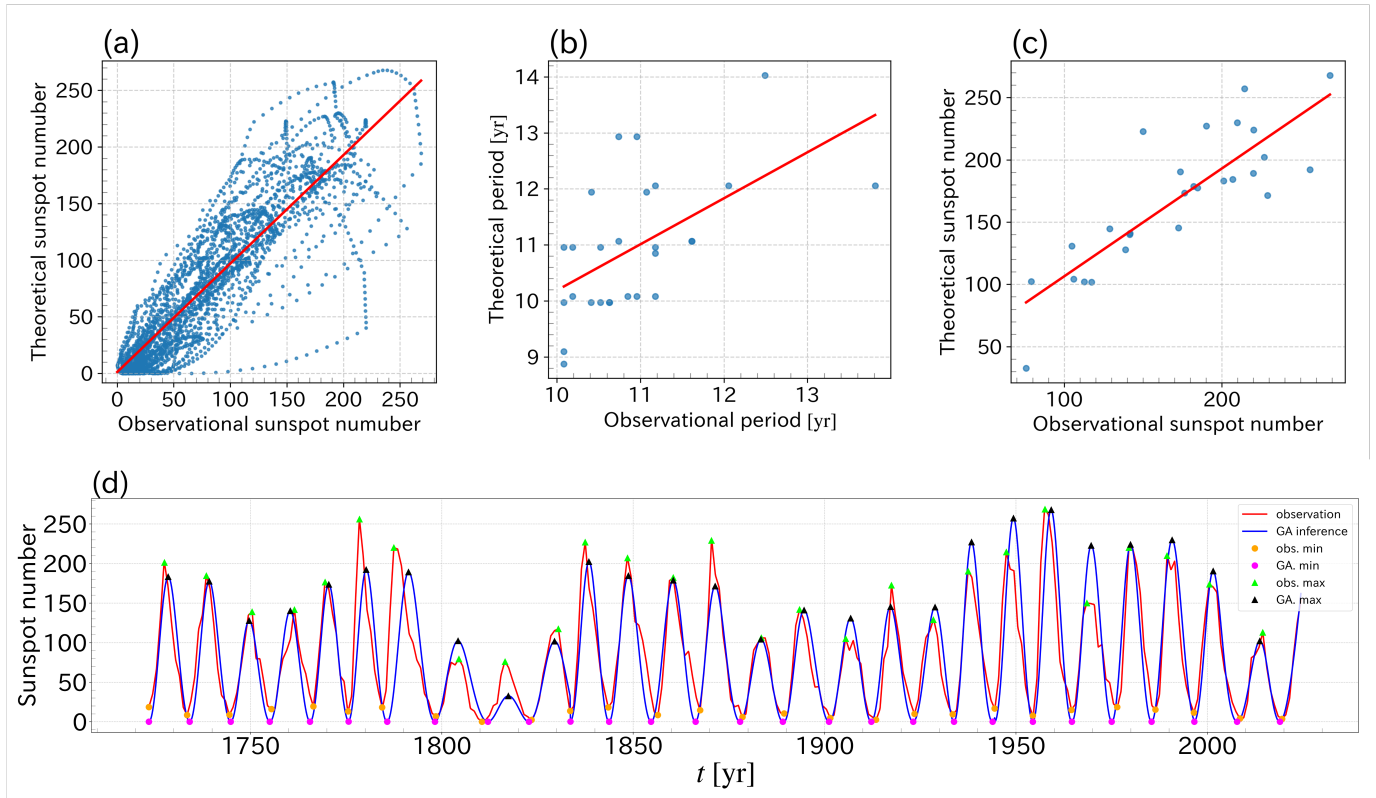


Figure 6. Statistical comparison of GA inference with observations. Panel a shows a scatter plot of SSN. The correlation coefficient is 0.876. Panel b shows the scatter plot of the cycle periods. The correlation coefficient is 0.566. The length of the cycle is measured by determining the minimum point, as indicated by the pink and orange circles in panel d. Panel c shows the correlation of SSN at the maximum period. The correlation coefficient is 0.842. The SSN at the maximum period is indicated by light green and black triangles for the observation and the GA inference, respectively.

directly incorporating the period or the position of the cycle minima into the fitness will improve the inference accuracy of u_0 and enhance the accuracy of period reproduction. We intend to reproduce the overall structure, but there is a possibility of using some representative value, such as the SSN, in the maximum and the cycle period. Furthermore, we just use the SSN in this study, but our algorithm can be extended to reproduce the global magnetic field observed in modern instrumentation. The choice of the initial condition is also possibly improved. We generate the initial condition for the 5-cycle unit independently. We can inherit the final state of a 5-cycle unit magnetic field to the next unit. This allows us to obtain smooth, continuous results for SSN,

u_0 , and s_0 , which we believe brings the model closer to reality.

As a further application, we plan to apply our method to the SSN obtained by isotope analysis, such as ^{14}C (H. Miyahara et al. 2004) and ^{10}Be (I. G. Usoskin et al. 2004) and historical documents (H. Hayakawa 2025).

ACKNOWLEDGMENTS

H.H. is supported by JSPS KAKENHI grant Nos. JP25H00673, JP25K22031, JP23K25906, JP21H04497, and JP21H04492 and MEXT as a Programme for Promoting Researchers on the Supercomputer Fugaku (JPMXP1020230504).

APPENDIX

A. NUMERICAL METHOD

We describe the second-order Total Variation Diminishing (TVD) Runge-Kutta method (C.-W. Shu & S. Osher 1988). We follow the procedure shown below to advance a time step. We use an arbitrary variable ϕ and we assume

to solve an equation as

$$\frac{\partial\phi}{\partial t} = R(\phi), \quad (\text{A1})$$

where R is an arbitrary operator. First, we use the forward Euler method to derive $\phi^{(a)}$ and $\phi^{(b)}$ from n -th step value ϕ^n . $\phi^{(a)}$ and $\phi^{(b)}$ are given as

$$\phi^{(a)} = \phi^n + \Delta t R(\phi^n), \quad (\text{A2a})$$

$$\phi^{(b)} = \phi^{(a)} + \Delta t R(\phi^{(a)}). \quad (\text{A2b})$$

Second, we calculate ϕ^{n+1} by taking the average of the $\phi^{(b)}$ and ϕ^n values obtained. ϕ^{n+1} is given as

$$\phi^{n+1} = \frac{1}{2}\phi^n + \frac{1}{2}\phi^{(b)}. \quad (\text{A3})$$

Using this scheme, equation(1) can be solved with satisfying the TVD condition.

REFERENCES

- Babcock, H. W. 1961, *ApJ*, 133, 572, doi: [10.1086/147060](https://doi.org/10.1086/147060)
- Beyer, H.-G., & Schwefel, H.-P. 2002, *Natural computing*, 1, 3. <https://doi.org/10.1023/A:1015059928466>
- Charbonneau, P. 2020, *Living Reviews in Solar Physics*, 17, 4, doi: [10.1007/s41116-020-00025-6](https://doi.org/10.1007/s41116-020-00025-6)
- Choudhuri, A. R. 1992, *A&A*, 253, 277
- Choudhuri, A. R., & Karak, B. B. 2009, *Research in Astronomy and Astrophysics*, 9, 953, doi: [10.1088/1674-4527/9/9/001](https://doi.org/10.1088/1674-4527/9/9/001)
- Choudhuri, A. R., Schussler, M., & Dikpati, M. 1995, *A&A*, 303, L29
- Deb, K., & Beyer, H.-G. 2001, *Evolutionary Computation*, 9, 197, doi: [10.1162/106365601750190406](https://doi.org/10.1162/106365601750190406)
- Dey, B., Sreedevi, A., & Karak, B. B. 2025, *The Astrophysical Journal*, 993, 196, doi: [10.3847/1538-4357/ae0ccb](https://doi.org/10.3847/1538-4357/ae0ccb)
- Dikpati, M., & Charbonneau, P. 1999, *ApJ*, 518, 508, doi: [10.1086/307269](https://doi.org/10.1086/307269)
- Eiben, A., Schut, M., & de Wilde, A. 2006, in *2006 IEEE International Conference on Evolutionary Computation*, 477–482, doi: [10.1109/CEC.2006.1688348](https://doi.org/10.1109/CEC.2006.1688348)
- Fan, Y. 2021, *Living Reviews in Solar Physics*, 18, 5, doi: [10.1007/s41116-021-00031-2](https://doi.org/10.1007/s41116-021-00031-2)
- Hale, G. E., Ellerman, F., Nicholson, S. B., & Joy, A. H. 1919, *ApJ*, 49, 153, doi: [10.1086/142452](https://doi.org/10.1086/142452)
- Hathaway, D. H. 2010, *Living Reviews in Solar Physics*, 7, 1, doi: [10.12942/lrsp-2010-1](https://doi.org/10.12942/lrsp-2010-1)
- Hayakawa, H. 2025, *arXiv e-prints*, arXiv:2502.14665, doi: [10.48550/arXiv.2502.14665](https://doi.org/10.48550/arXiv.2502.14665)
- Hotta, H., Bekki, Y., Gizon, L., Noraz, Q., & Rast, M. 2023, *SSRv*, 219, 77, doi: [10.1007/s11214-023-01021-6](https://doi.org/10.1007/s11214-023-01021-6)
- Hotta, H., & Yokoyama, T. 2010, *ApJ*, 709, 1009, doi: [10.1088/0004-637X/709/2/1009](https://doi.org/10.1088/0004-637X/709/2/1009)
- Jha, B. K., Karak, B. B., Mandal, S., & Banerjee, D. 2020, *The Astrophysical Journal Letters*, 889, L19, doi: [10.3847/2041-8213/ab665c](https://doi.org/10.3847/2041-8213/ab665c)
- Jiang, J. 2020, *ApJ*, 900, 19, doi: [10.3847/1538-4357/abaa4b](https://doi.org/10.3847/1538-4357/abaa4b)
- Jouve, L., Brun, A. S., Arlt, R., et al. 2008, *A&A*, 483, 949, doi: [10.1051/0004-6361:20078351](https://doi.org/10.1051/0004-6361:20078351)
- Karak, B. B. 2010, *ApJ*, 724, 1021, doi: [10.1088/0004-637X/724/2/1021](https://doi.org/10.1088/0004-637X/724/2/1021)
- Karak, B. B. 2023, *Living Reviews in Solar Physics*, 20, 3, doi: [10.1007/s41116-023-00037-y](https://doi.org/10.1007/s41116-023-00037-y)
- Karak, B. B., & Choudhuri, A. R. 2013, in *IAU Symposium, Vol. 294, Solar and Astrophysical Dynamos and Magnetic Activity*, ed. A. G. Kosovichev, E. de Gouveia Dal Pino, & Y. Yan, 433–438, doi: [10.1017/S1743921313002895](https://doi.org/10.1017/S1743921313002895)
- Kumar, P., Karak, B. B., & Vashishth, V. 2021, *ApJ*, 913, 65, doi: [10.3847/1538-4357/abf0a1](https://doi.org/10.3847/1538-4357/abf0a1)
- Leighton, R. B. 1969, *ApJ*, 156, 1, doi: [10.1086/149943](https://doi.org/10.1086/149943)
- Lemerle, A., & Charbonneau, P. 2017, *ApJ*, 834, 133, doi: [10.3847/1538-4357/834/2/133](https://doi.org/10.3847/1538-4357/834/2/133)
- Maunder, E. W. 1904, *MNRAS*, 64, 747, doi: [10.1093/mnras/64.8.747](https://doi.org/10.1093/mnras/64.8.747)
- Miyahara, H., Masuda, K., Muraki, Y., et al. 2004, *SoPh*, 224, 317, doi: [10.1007/s11207-005-6501-5](https://doi.org/10.1007/s11207-005-6501-5)
- Miyahara, H., Tokanai, F., Moriya, T., et al. 2021, *Scientific Reports*, 11, 5482, doi: [10.1038/s41598-021-84830-5](https://doi.org/10.1038/s41598-021-84830-5)
- Parker, E. N. 1955, *ApJ*, 122, 293, doi: [10.1086/146087](https://doi.org/10.1086/146087)
- Schou, J., Antia, H. M., Basu, S., et al. 1998, *ApJ*, 505, 390, doi: [10.1086/306146](https://doi.org/10.1086/306146)

Shu, C.-W., & Osher, S. 1988, *Journal of Computational Physics*, 77, 439,

doi: [https://doi.org/10.1016/0021-9991\(88\)90177-5](https://doi.org/10.1016/0021-9991(88)90177-5)

Usoskin, I. G., Mursula, K., Solanki, S., Schüssler, M., & Alanko, K. 2004, *A&A*, 413, 745,

doi: [10.1051/0004-6361:20031533](https://doi.org/10.1051/0004-6361:20031533)

Waldmeier, M. 1935, *Astronomische Mitteilungen der Eidgenössischen Sternwarte Zurich*, 14, 105

Waldmeier, M. 1939, *Astronomische Mitteilungen der Eidgenössischen Sternwarte Zurich*, 14, 470

WDC-SILSO, Royal Observatory of Belgium. 2025, Yearly Mean Total Sunspot Number,,

<https://www.sidc.be/SILSO/infosnytot>

doi: [10.24414/qnza-ac80](https://doi.org/10.24414/qnza-ac80)